Design and Optimization of Electrical Parameters of Perovskites-based Thin Film Solar Cell

Muhammad Muneeb Khan , Sadiq Ahmad * , Ali Hassan * , And Furqan Shaukat

Posted Date: 2 April 2024

doi: 10.20944/preprints202404.0138.v1

Keywords: Electrical Parameters; Perovskite; Optimization; Renewable Power; SCAPS-1D; PVSyst; Solar Module; Solar Cell

Article

Design and Optimization of Electrical Parameters of Perovskites-Based Thin Film Solar Cell

Muhammad Muneeb Khan [1,2,†], Sadiq Ahmad [3,*,†], Ali Hassan [4,*,†] and Furqan Shaukat [5,†]

[1] Department of Electrical & Comp. Engg, COMSATS University Islamabad, Wah Campus, 47040, Pakistan; muneebkhan196@yahoo.com
[2] Department of Electrical Engineering & Technology, Institute of Southern Punjab, Multan, 6000, Pakistan;
[3] Department of Electrical & Comp. Engg, COMSATS University Islamabad, Wah Campus, 47040, Pakistan; engrsadiqahmad@ciitwah.edu.pk
[4] Department of Electrical and Computer Engineering, University of Michigan-Dearborn, Michigan, 48135, USA; alihssn@umich.edu
[5] Faculty of Electronics and Electrical Engineering, University of Engineering and Technology, Taxila, 47080, Pakistan; furqan.shoukat@uettaxila.edu.pk
* Correspondence: engrsadiqahmad@ciitwah.edu.pk; alihssn@umich.edu;
† These authors contributed equally to this work.

Abstract: This paper investigates an innovative photovoltaic cell configuration, denoted as "$Au/CuSCN/RbGeI_3/CdTe/ZnO/TiO_2/FTO$", using SCAPS-1D simulation. The research focuses on optimizing device performance by analyzing key components, including ZnO as the electron transport layer (ETL), $RbGeI_3$ as the perovskite absorber layer, $CuSCN$ as the hole transport layer (HTL), and $CdTe$ as the active buffer layer. A comparison is made with the standard "$Au/CuSCN/CH_3NH_3SnI_3/CdTe/ZnO/TiO_2/FTO$" configuration under dark and illuminated conditions. Through an in-depth investigation involving temperature effects, generation rate analysis, $RbGeI_3$ absorber layer thickness, N_d level, and interface defect levels, an optimized design for a unit area is achieved. The proposed solar cell demonstrates outstanding performance metrics, including an open circuit voltage (V_{oc}) of $0.94V$, a short circuit current density (J_{sc}) of $34.52mA/cm^2$, a fill factor (FF) of 77.77%, and an energy conversion efficiency (η) of 25.40%. These values significantly outperform the reference models with energy conversion efficiencies of 10.11% and 21.09%. Real-world applicability is validated by implementing these optimized characteristics in a photovoltaic system for Pakistan's geographical location using PVSyst software. The suggested solar cell achieves a remarkable performance ratio (PR) of 85.6%, surpassing the PR of the reference basic solar cell model at 83%. The findings of this research offer a promising and superior solar cell design, incorporating innovative materials and optimization techniques to achieve exceptional energy conversion efficiency and overall performance. This study's outcomes have the potential to advance photovoltaic technology and contribute to sustainable energy solutions worldwide.

Keywords: electrical parameters; perovskite; optimization; renewable power; SCAPS-1D; PVSyst; solar module; solar cell

1. Introduction

Organic-inorganic hybrid lead halides have a very high coefficient of absorption, simple structure synthesis, variation in the band gap, extended length of diffusion, and processability of a solution, among other properties [1,2]. Kojima et al. reported their initial use in 2009 where solar cell efficiency reaches up to 3.8% [3]. Power conversion efficiencies (PCEs) have grown by up to 25.5% during the last ten years [4]. However, one of the main obstacles to perovskite commercialization is thought to be the inclusion of lead, a toxin by nature. In the search for alternatives to lead, scientists have looked into certain additional metal cations with divalent electrons, such as Sn^{2+} and Ge^{2+}, its outermost shell comparable with Pb^{2+} and Ga^{2+} oxidation state [5]. When Sn^{2+} is used as the metal cation with divalent electrons in place of Pb^{2+}, the perovskite crystal structure is not disrupted because Sn^{2+} carries a smaller ionic radius (1.35) than Pb^{2+} (1.49) [6,7]. Because of their narrower band gaps, Sn-based perovskites exhibit higher theoretical efficiency [8]. Sabba et al. investigated different band gap lengths of several stannic-based perovskite materials of the solar cells, including $CsSnI_3$,

 doi:10.20944/preprints202404.0138.v1

$CsSnI_2\,Br$, $CsSnIBr_2$, and $CsSnBr_3$ [9]. $CsSnI_3$ in the mentioned solar cell materials is the best material used in perovskite solar cell (PSC) layers because of its narrow band gap (1.27 eV). This material-based PSC projected a power conversion efficiency (PCE) of 23% and it demonstrated extremely good optoelectronic characteristics. Due to the readily occurring oxidation of Sn^{2+} to Sn^{4+}, most Stannic-based PSCs have significantly limited efficiency as they are prone to degradation in typical room environments. Sn vacancies have extremely low formation energy [10–12].

Sn-based perovskites exhibit p-type metallic behavior due to self-doping caused by the low energy of formation and easy release of oxidizing electrons, converting Sn^{2+} to Sn^{4+}. Ge^{2+}, which normally has an ionic radius of 0.73, is smaller compared to Sn^{2+} and Pb^{2+}, making it another viable option to replace Pb^{2+} as a divalent metal cation with electrons [13].

In comparison to all Pb and Sn-based PSCs, Ge-based perovskites exhibit higher conductivity. G. Pindolia et al. showed a maximum PCE of 18.3% by simulating $CsGeI_3$ PSCs with SCAPS [14,15]. The PSCs were modeled using various electron transport layers (ETLs), and they found that C_{60} and SnO_2 had PCEs of 8.45% and 8.46%, respectively [16]. Saikia et al. discovered the effects of thickness, concentration defects, and concentration doping on a $CsGeI_3$-based PSC [17].

Various physical properties of $RbGeI_3$-based perovskites in a three-dimensional cubic structure with $Pm-3m$ space groups, along with other optoelectronic, thermodynamic, and mechanical properties, were explored in [17]. Different electronic properties and characteristics, notably their structure and magnetic properties, of cubic $RbGeI_3$ and $RbDyO_3$ perovskites were investigated in [18–20]. Optical analysis, first principles, structural, and electrical characteristics of $RbGeI_3$ PSCs were conducted by Jong et al. The PBEsol functional was used to compute various parameters, including dielectric constants at static and high frequencies, and other mass calculations of electrons and holes, along with band gap length, lattice constant, and tolerance factor [21,22].

Thiele et al. in [23] investigated the heating and thermal behavior of $RbGeI_3$ using X-ray diffraction technology and spectroscopy. Researchers have been significantly concerned about the instability caused by organic chemicals in PSCs [23–25]. Spiro-OMeTAD, a widely used modern hole transport material (HTM), requires a laborious five-step production process, including mixing, heating, chemical preparation, layer design, and drying, resulting in a yield of under 40%.

In the synthesis process, changes of cations such as bromination, nucleophilic and electrophilic exchange in cyclization, as well as Grignard and Hartwig Buchwald reactions, were employed [26,27].

Spiro-OMeTAD fabrication demands less temperature like $(195.15K)$ at the extremely difficult condition of reagent. Sublimation processes, which are quite expensive, are necessary to create high-purity spiro-OMeTAD [20,28]. In ambient temperature and pressure conditions and under normal illumination conditions organic-based charge transport materials (CTMs) become unstable [15,29]. Therefore, inorganic charge transport materials were investigated, which includes the use of NiO [30], the use of TiO_2 [31], and the use of SnO_2 [29,32]. The inorganic CTMs are inexpensive since the fabrication process is straightforward. When compared to organic CTMs, inorganic CTMs exhibit greater chemical and thermodynamic stability [33]. In addition, in comparison to organic, the inorganic CTMs have a long length of band gap, charge carriers' high mobility, and are transparent for infrared and ultraviolet radiation visibility [34–40]. The authors in [41], used the same concept by utilizing the SCAPS-1D to calculate the values of V_{mpp}, I_{mpp}, which is then used for the analysis of solar energy via PVSyst.

1.1. Contribution

This research represents a significant step forward in the realm of photovoltaics, offering a highly efficient and environmentally conscious solar cell design. The overall research contributions are summarized as follows:

- A novel, efficient solar cells configuration is suggested in this research work that is inert to the environmental impact $Au/CuSCN/RbGeI_3/CdTe/ZnO/TiO_2/FTO$ ".

 doi:10.20944/preprints202404.0138.v1

- This research introduces an optimized solar cell model featuring the environmentally friendly $RbGeI_3$ perovskite absorber layer, leading to a significant improvement in power conversion efficiency.
- By incorporating advanced inorganic transport materials like TiO_2, ZnO, and the inorganic hydrogen transport material $CuSCN$, the solar cell achieves an extraordinary power conversion efficiency of 25.40%.
- Meticulous optimization of critical properties, such as temperature effects, generation rate analysis, $RbGeI_3$ absorber layer thickness, N_d level, and interface defect levels, results in an exceptional fill factor (FF) of 77.77%.
- Real-world applicability is confirmed through simulations using the powerful PVSyst software, with the solar cell demonstrating an outstanding performance ratio (PR) of 85.64%, making it a promising candidate to meet substantial daytime energy demands.

1.2. Organization of the Paper

In Section 2, existing solutions and literature related to PV cell modeling and simulation are revealed. The subsequent section, Section 3, unveils an optimized solar cell model with the exceptional $RbGeI_3$ perovskite absorber layer and presents a discussion of the impressive results. Finally, in Section 4, the paper glimpses the promising future of this research, envisioning a revolution in sustainable energy solutions.

2. Modeling and Simulation Parameters

The solar spectrum restricts the effectiveness of a single solar cell, but it is possible to build improvements by stacking two separate band gaps to absorb more energy packets of photons at the top and bottom. To evaluate and optimize these advanced solar cell designs, researchers rely on specialized computer-based software. Some popular choices include SETFOS, SCAPS-1D, SILVACO, COMSOL, and ATLAS. Among these, SCAPS-1D stands out for its user-friendly interface and remarkable versatility. It excels in simulating solar cells under various lighting conditions, from bright sunlight to complete darkness. The authors in [14,41] utilize the power of SCAPS-1D version 3.3.10 to explore the potential of a heterostructure system with multiple layers. This research work unlocks the secrets of solar cell optimization, paving the way for greater efficiency and sustainability.

In the initial simulation, "$Au/CuSCN/CH_3NH_3SnI_3/CdTe/ZnO/TiO_2/FTO$" PSC structure is employed. The initial structure input parameters and parameters for inter-facial defects of layers in material, as shown in Table 1 are derived from theories and existing research.

At a temperature of $300K$, a steady illumination of $1000Wm^2$ at AM 1.5G is proposed. Electrons and holes have a thermal velocity of 10^7 cm/s. By incorporating a $CdTe/RbGeI_3$ interface layer and a $RbGeI_3/CuSCN$ interface layer, a more realistic PSC is mimicked. For both interfaces, a neutral defect density of 10^{16}cm^{-3} with a characteristic energy of $0.1eV$ is used. The work function of back contact Au is calculated to be $5.10eV$. We retained the donor (N_D) and acceptor (N_A) doping concentrations of $RbGeI_3$ at 10^9cm^{-3}.

In the literature, various factors are documented that can affect the solar cell's performance, including open circuit voltage, fill factor (FF), short circuit current density, power conversion efficiency (PCE), quantum efficiency, band gap energy, and voltage-to-current characteristics. In SCAPS-1D software, it is very easy to analyze all these factors through the basic Poisson's equation, which gives the relation of charges to electrostatic potential as discussed in Eq. (1).

$$-\frac{\partial}{\partial x}\{-\varepsilon(x)\frac{\partial V}{\partial x}\} = q\Big[p(x) - n(x) + N_D^+(x) - N_A^-(x) + P_t(x) - N_t(x)\Big] \tag{1}$$

 doi:10.20944/preprints202404.0138.v1

For the analysis of electrons and holes generations and recombination, as well as the drift and diffusion, the continuity equations can be utilized which is given by

$$\frac{\partial n}{\partial t} = \frac{1}{q}\frac{\partial J_n}{\partial x} + G_n - R_n \tag{2}$$

Table 1. Simulation parameters of designed solar cell used for simulation

Parameters	$CuSCN$	$RbGeI_3$	$CH_3NH_3SnI_3$	$CdTe$	ZnO	TiO_2	FTO
$W(\mu m)$	0.10	0.40	4.72	0.023	0.045	0.03	0.50
E_g (eV)	3.40	1.31	1.35	1.56	3.37	3.20	3.20
χ (eV)	1.90	3.90	4.17	4.40	4.35	4.0	4.0
ε_r	10.0	23.01	6.50	9.40	10.0	100	9.00
$N_C(cm^{-3})$	2.20x10^{18}	2.80x10^{19}	1.00x10^{18}	8.00x10^{17}	2.22x10^{18}	2.00x10^{20}	1.80x10^{19}
$N_V(cm^{-3})$	1.80x10^{19}	1.40x10^{19}	1.00x10^{19}	1.80x10^{19}	1.78x10^{19}	1.00x10^{21}	2.20x10^{18}
$V_e(cm/s)$	1.00x10^{7}	1.00x10^{7}	1.00x10^{7}	1.00x10^{7}	1.00x10^{7}	1.00x10^{7}	1.00x10^{7}
$V_p(cm/s)$	1.00x10^{7}	1.00x10^{7}	1.00x10^{7}	1.00x10^{7}	1.00x10^{7}	1.00x10^{7}	1.00x10^{7}
$\mu_e(cm^2/(Vs))$	1.00x10^{4}	2.86x10^{1}	1.60x10^{0}	3.20x10^{2}	1.00x10^{2}	6.00x10^{-3}	2.00x10^{1}
$\mu_p(cm^2/(Vs))$	1.00x10^{-2}	2.73x10^{1}	1.60x10^{0}	4.10x10^{1}	2.50x10^{1}	6.00x10^{-3}	1.00x10^{1}
$N_D(cm^{-3})$	0.00x10^{0}	1.00x10^{9}	0.00x10^{0}	0.00x10^{0}	1.00x10^{20}	5.06x10^{19}	1.00x10^{19}
$N_A(cm^{-3})$	1.00x10^{16}	1.00x10^{9}	3.20x10^{15}	2.00x10^{14}	0.00x10^{0}	0.00x10^{0}	0.00x10^{0}

$$\frac{\partial n}{\partial t} = \frac{1}{q}\frac{\partial J_p}{\partial x} + G_p - R_p \tag{3}$$

Eq. (2), (3) represents the continuity equations for electrons and holes simultaneously. In Eq. (1), (2), and (3), q is used to represent charge, the permittivity of dielectric is represented by ε, V is the potential, free holes, and electron concentration is represented by $p(x)$ and $n(x)$ respectively. The ionized donor and acceptor concentration is represented by $N_D^+(x)$, and $N_A^-(x)$, while the density of the hole and electron trap is represented by $P_t(x)$, and $N_t(x)$ respectively. Similarly, the density of electron and hole current is represented by J_n, and J_p. The electron and hole generation and their recombination rate are mathematically represented by G_n, G_p, R_n and R_p respectively.

3. Results and Discussions

The simulation was meticulously conducted using the SCAPS-1D simulator at an operating temperature of 300K under $AM1.5G1$ solar light conditions. Series resistance was set to zero ohms, while shunt resistance was set to infinity, ensuring precise and reliable analysis. The current research underwent rigorous validation through SCAPS-1D modeling, reinforcing the credibility of the findings. Building on this solid foundation, the investigation delved into the effects of replacing the traditional $CH_3NH_3SnI_3$ absorber layer with $RbGeI_3$. The PV cell performance was systematically examined, uncovering the potential of this innovative approach.

3.1. Basic Solar Cell Validation through SCAPS

A basic simulation was carried out using the SCAPS-1D software to validate the performance of the PSC, specifically the solar cell model "$Au/CuSCN/CH_3NH_3SnI_3/CdTe/ZnO/TiO_2/FTO$". The simulation yielded impressive open circuit voltage (V_{oc}) and short circuit current density (J_{sc}) values, standing at 0.81V and 33.57mA/cm^2, respectively. Notably, the fill factor (FF) exhibited a remarkable value of 77.17%, while the power converting efficiency reached an impressive 21.09%. The recorded results, depicted in the current density to voltage curve shown in Figure 1, perfectly align with previously published works, affirming the accuracy and reliability of our simulation.

 doi:10.20944/preprints202404.0138.v1

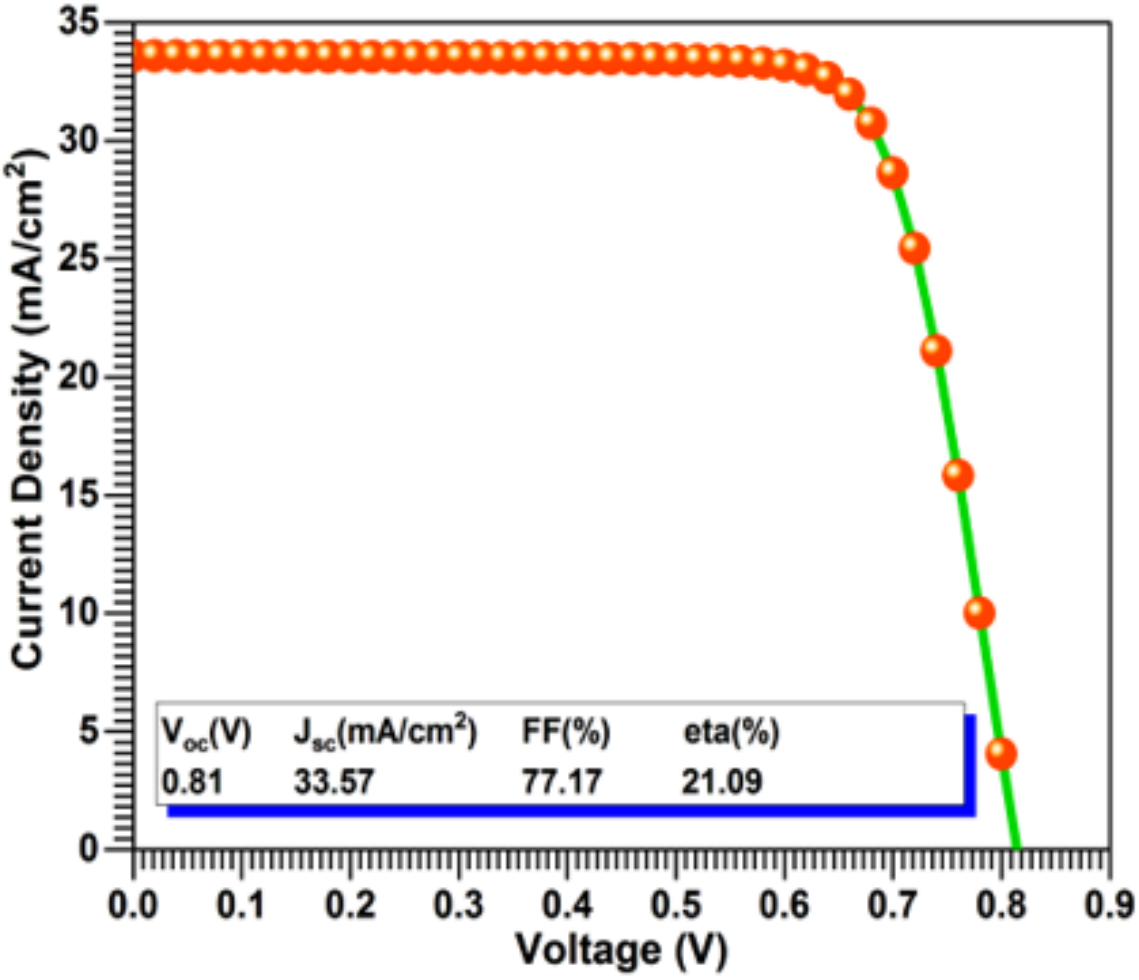

Figure 1. Initial $J-V$ characteristics curve of the proposed model

3.2. Band Gap Energy Diagram

The simulation results showcase an impressive optimization and design of absorber layers in PV cells. The materials used for these layers include organic compounds, metals, and anions, which play a crucial role in determining the band gap energy of PV cells. The focus of the study was on the band gap energy, a critical factor in determining the PV cell's performance. The $RbGeI_3$ based PV cell demonstrated a type II broken band gap with a band gap length of approximately $1.55eV$, aligning perfectly with expectations. Notably, the PSC exhibited a distinctive characteristic with a single junction within the overall band gap. The introduction of the $RbGeI_3$ based PV cell led to a remarkable increase in the open circuit voltage (V_{oc}), elevating it from 0.80 to an impressive $0.94V$.

 doi:10.20944/preprints202404.0138.v1

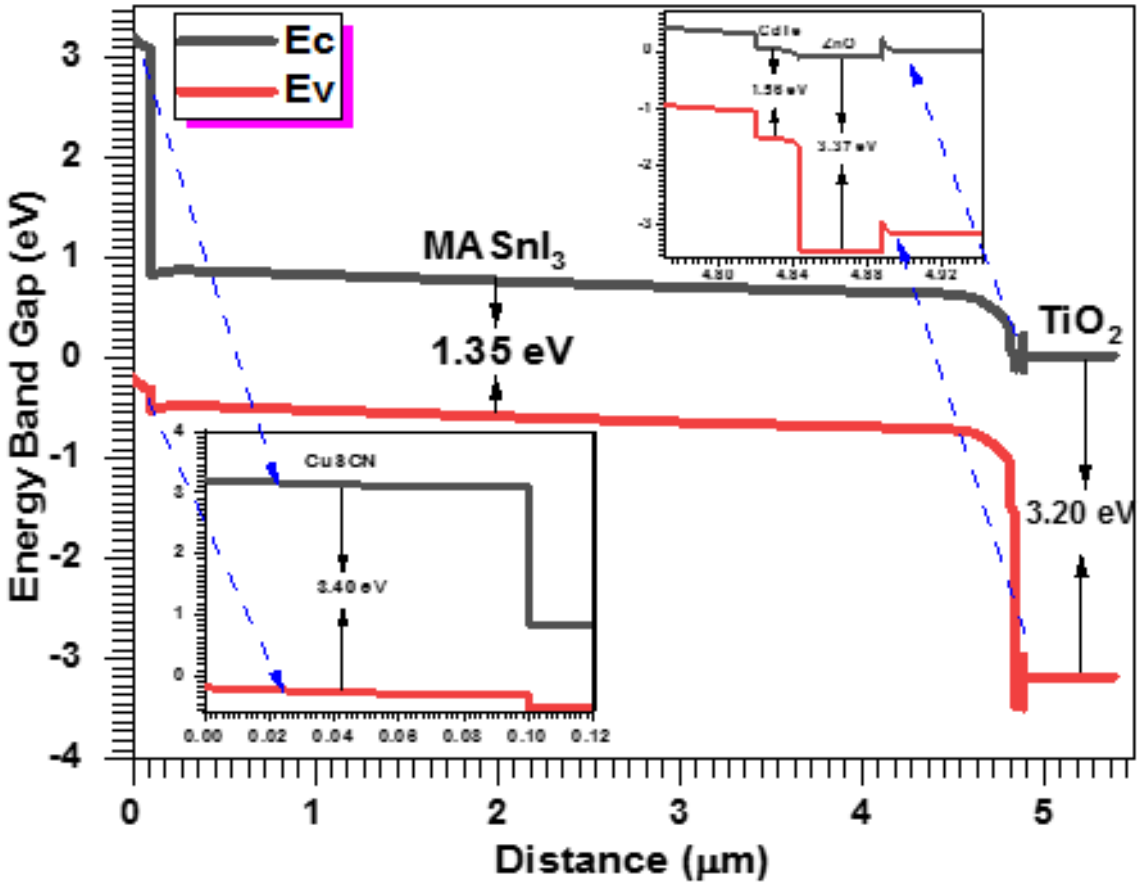

Figure 2. Band gap Energy diagram

3.3. Current Density-Voltage Characteristic Curve under Illumination and Dark

The simulation results provide valuable insights into the performance of the solar cell. The focus was on the current density to voltage characteristic curve of the basic model of $CH_3NH_3SnI_3$-based PSC, as depicted in Figure 2. The key metrics obtained from the $J-V$ curve in Figure 2 of the current model are open circuit voltage (V_{oc}), $0.81V$, short circuit current density (J_{sc}) of $33.57mA/cm^2$, fill factor (FF) of 77.17%, and PCE of 21.09%. When exposed to sunlight, the solar cell experiences electron movement, leading to the current generation. However, in darkness, no such action occurs, resulting in no current generation. A comparison of the solar cell's response to light and dark conditions is illustrated in Figure 3.

 doi:10.20944/preprints202404.0138.v1

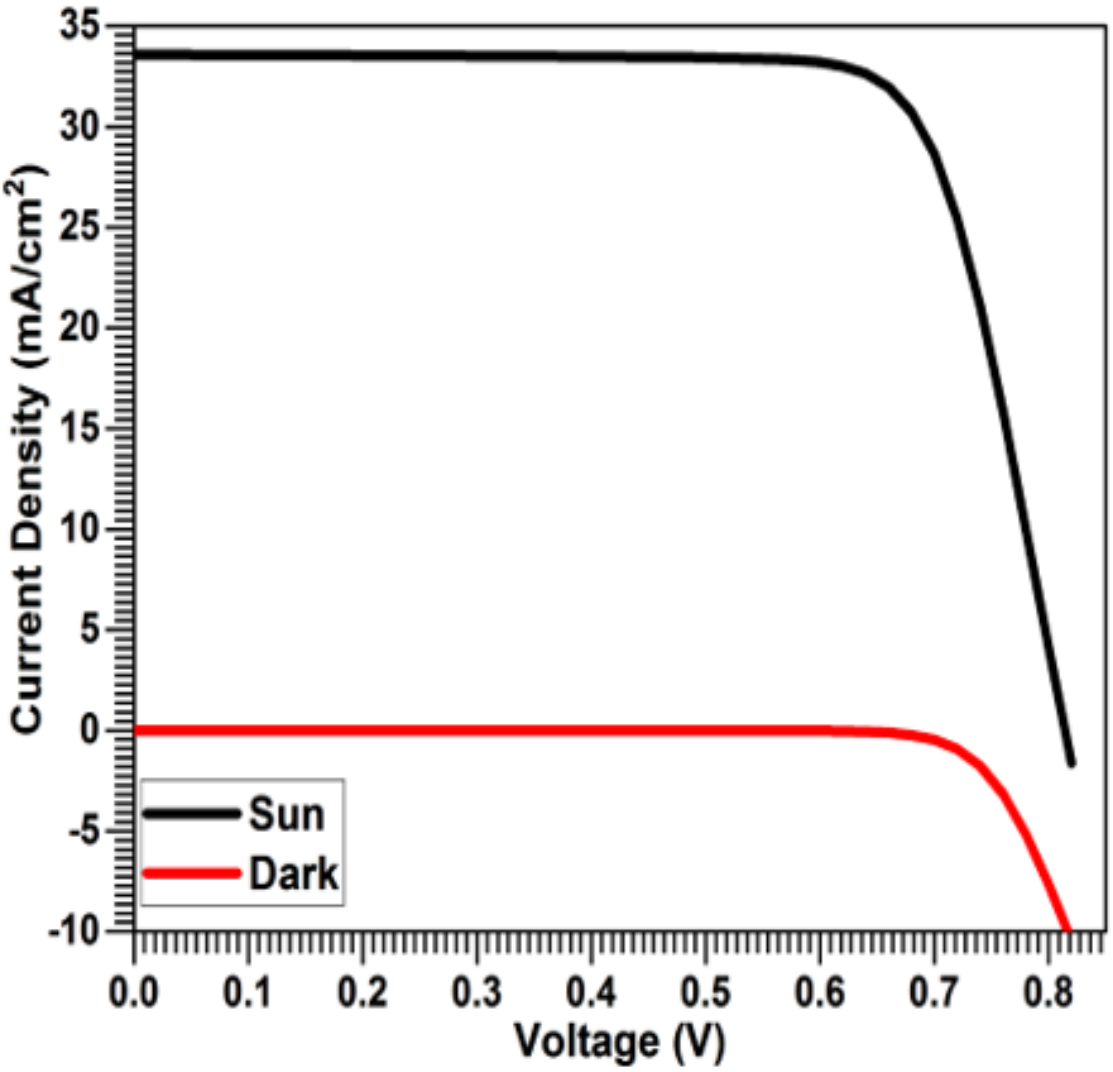

Figure 3. $J-V$ Characteristics curve under dark and sun

3.4. $J-V$ Characteristic Curve Analysis for $MASnI_3$ and $RbGeI_3$

PV cell performance is embellished through current density to voltage characteristic curve which is depicted in Figure 4. Figure 4 shows a comparison characteristic curve between the current simulated model "$Au/CuSCN/CH_3NH_3SnI_3/CdTe/ZnO/TiO_2/FTO$" and proposed PSC model "$Au/CuSCN/RbGeI_3/CdTe/ZnO/TiO_2/FTO$".

Preprints.org (www.preprints.org) | NOT PEER-REVIEWED | Posted: 2 April 2024 doi:10.20944/preprints202404.0138.v1

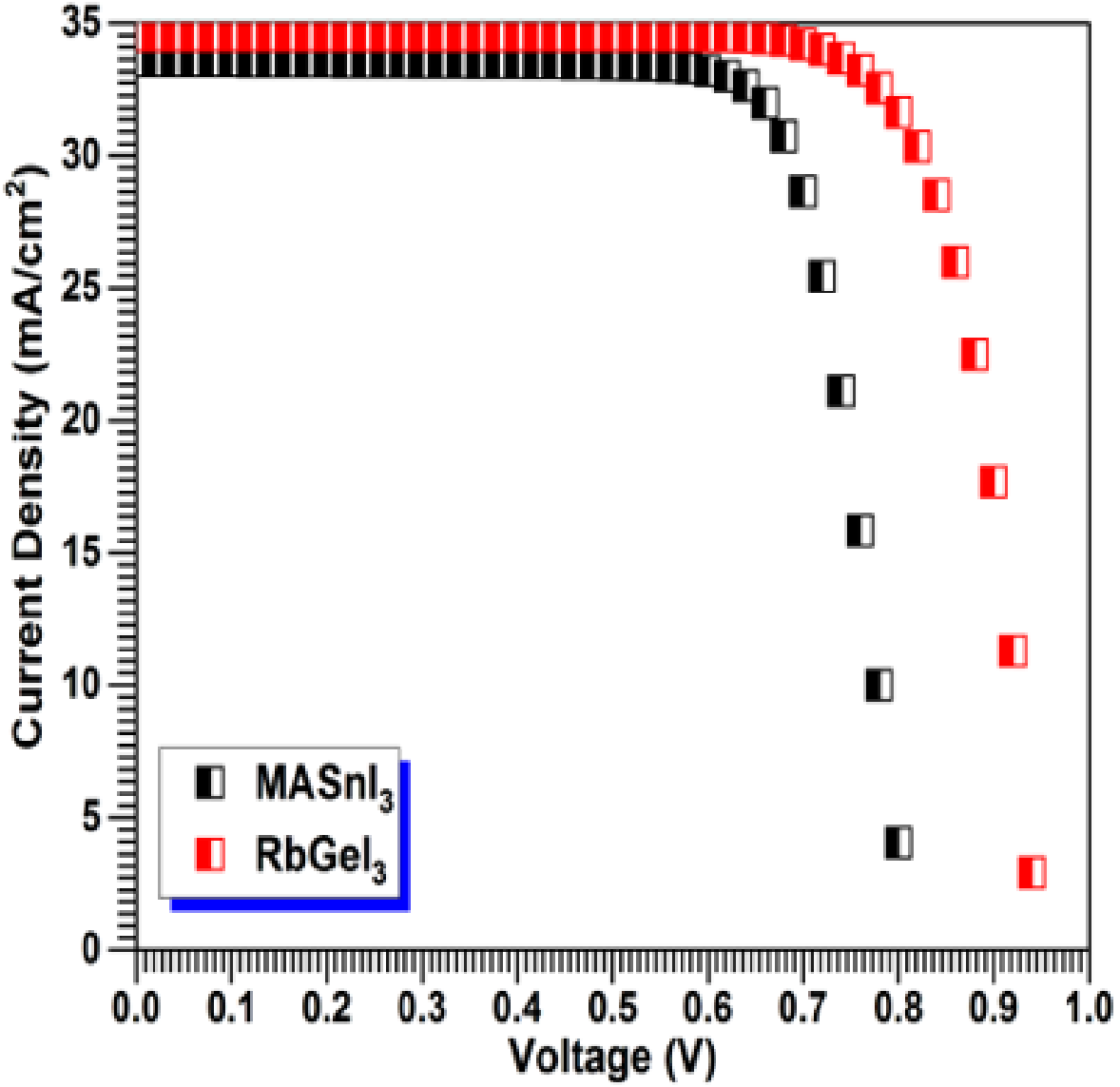

Figure 4. $J-V$ curve of $MASnI_3$ vs $RbGeI_3$-based solar cells

From the given characteristic curve, it can be easily noted that the proposed PSC model is given a value of open circuit voltage of $0.94V$ and a value of short circuit current density of $34.52mA/cm^2$. Based on these values, the fill factor is calculated as 77.77%, and the PCE is calculated as 25.4%, which are summed up in Table 2. The value of open circuit voltage in the legacy model is recorded as $0.81V$ and the short circuit current density is $33.57mA/cm^2$, which is given a fill factor of 77.17% and a PCE of 21.09%. In conclusion, it can be seen from Figure 4 and from Table 2, that there is a comprehensive improvement in the PCE and in the fill factor.

Table 2. Characteristics parameters of $MASnI_3$ vs $RbGeI_3$-based solar cells

Solar cell Model	V_{oc} (V)	J_{sc} (mA/cm^2)	$FF(\%)$	$\eta(\%)$	Reference
$CuSCN/CH_3NH_3SnI_3$ $/CdTe/ZnO/TiO_2/FTO$	0.81	33.57	77.17	21.09	[41]
SpiroOMeTAD/$RbGeI_3$ $/TiO_2/FTO$	0.53	28.89	63.68	10.11	[14]
$CuSCN/RbGeI_3$ $/CdTe/ZnO/TiO_2/FTO$	0.94	34.52	77.77	25.40	Proposed

 doi:10.20944/preprints202404.0138.v1

3.5. Temperature Effects on PV Cell Performance

The simulation was conducted again to examine the influence of operating temperature on solar device performance. Temperatures ranged from 290K to 340K. At the lowest temperature, i.e., 290K, the value of V_{oc} was recorded as 0.8135V, J_{sc} was 33.9027mA/cm^2, FF was 70.208%, and efficiency η was 14.846%. Due to the lower temperature, the heating impact on the solar cell is minimal, which increases the efficiency to 14.846%. However, when the temperature increases from 280K to 340K, all of the parameters are significantly influenced, as shown in Figure 5.

At 290K, the V_{oc} recorded to 1.4823V, J_{sc} as 34.5250mA/cm^2 , FF as 49.73%, and PCE η as 25.45%. Similarly, at 300K, the V_{oc} recorded to 1.4857V, J_{sc} as 34.5252mA/cm^2, FF as 49.52%, and PCE η as 25.40%. In the same way, by increasing temperature more up to 340K, its characteristics parameters were affected, as at 340K, the V_{oc} measured to 1.4495V, J_{sc} as 34.5261mA/cm^2, FF as 50.09%, and PCE η as 25.07%. The rise in temperature increases the collision of electrons and holes, which slows the flow of charges. As a result, there is less generation of potential and thus a decrease in efficiency. Figure 5 depicts the detrimental effect of rising temperatures on the $J-V$ curve.

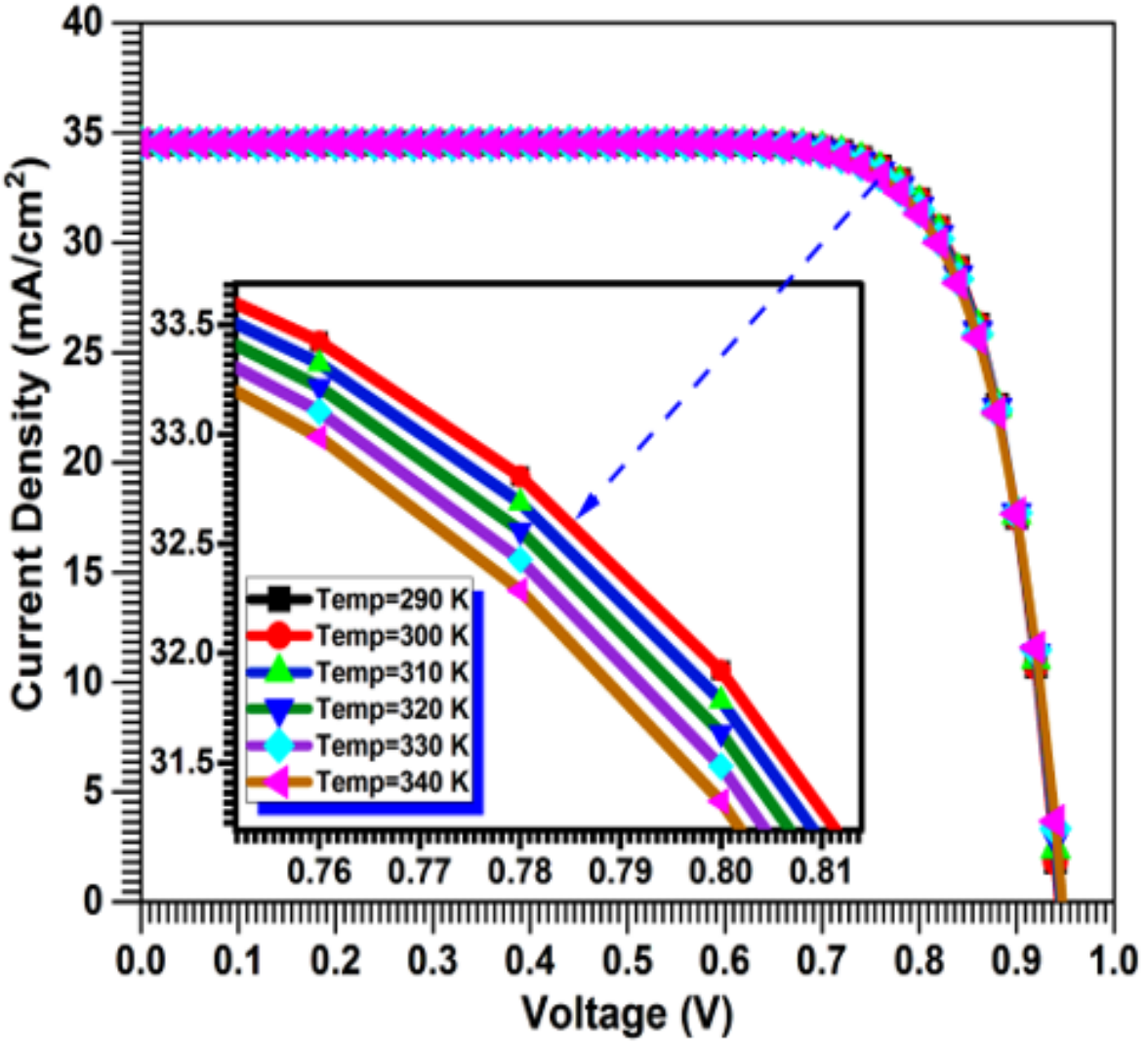

Figure 5. Temperature effect on $I-V$ characteristics curve of $RbGeI_3$-based solar cell

Rising temperature has a negative effect not only on the parameters of the characteristic (V_{oc}, J_{sc}, FF, and η) but also on the quantum efficiency. Quantum efficiency (QE) is defined as the ratio of carriers collected by the solar cell to the number of photons incident on the solar cell. As the

 doi:10.20944/preprints202404.0138.v1

temperature rises, its curve falls, implying that the ratio is decreasing, implying that the number of carriers collecting on the surface of the solar device is decreasing, as illustrated in Figure 6.

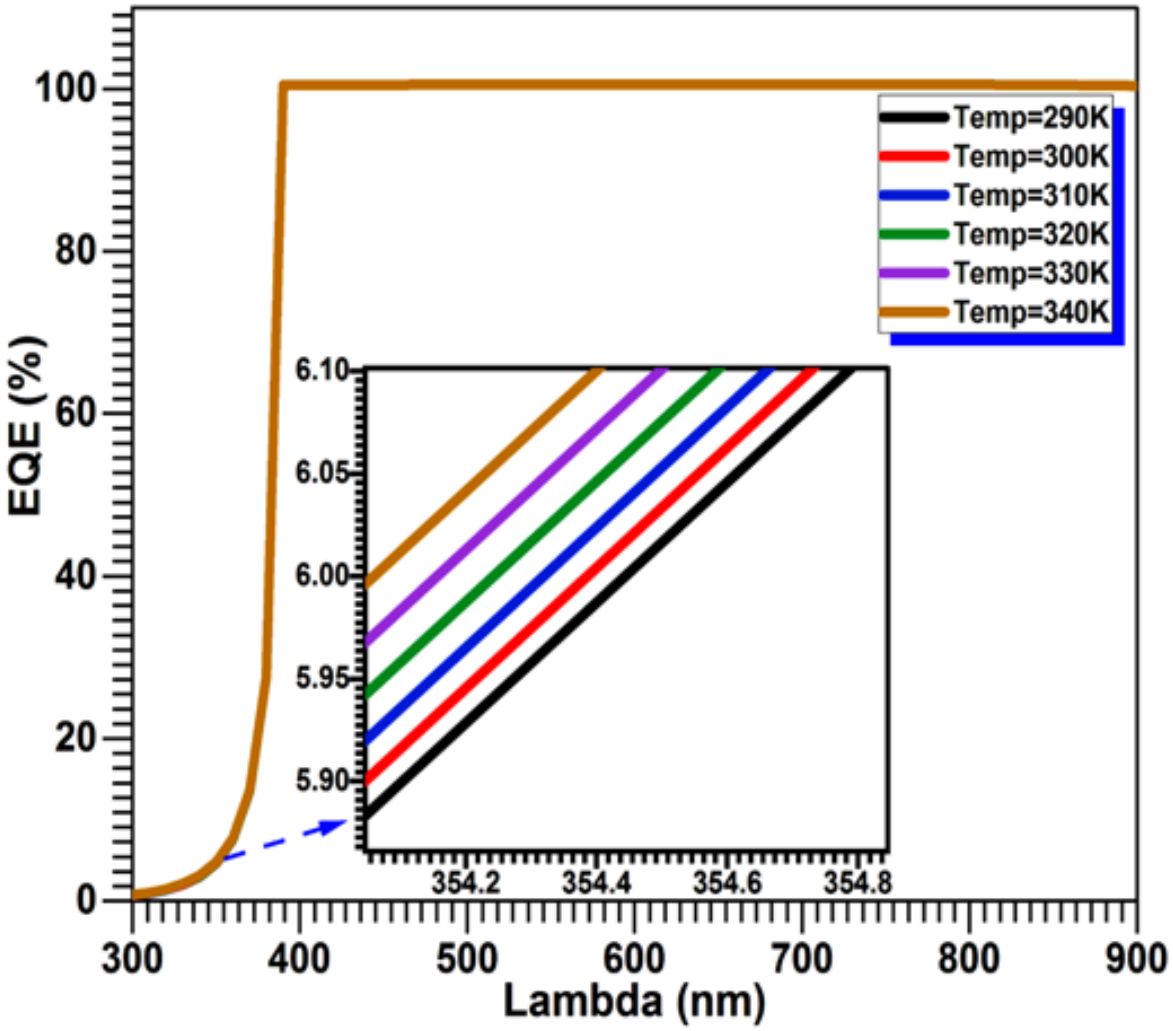

Figure 6. Temperature effect on quantum efficiency curve of $RbGeI_3$-based solar cell

3.6. Generation Rate Analysis of $RbGeI_3$ based Solar Cell

The connection between carrier generation and their recombination ($cm^{-3}s$) with photon's diffusion length in meters is shown in Figure 7 and 8 for the proposed PSC. Carrier generation and its recombination's maximum up to G_{eh} of $1.54 \times 10^{22} cm^{-3}s$ are discovered already at $4.15m$ as shown in Figure 7. It has been discovered that as the carrier's diffusion length rises, so does recombination, which may damage the effectiveness of PV cells.

 doi:10.20944/preprints202404.0138.v1

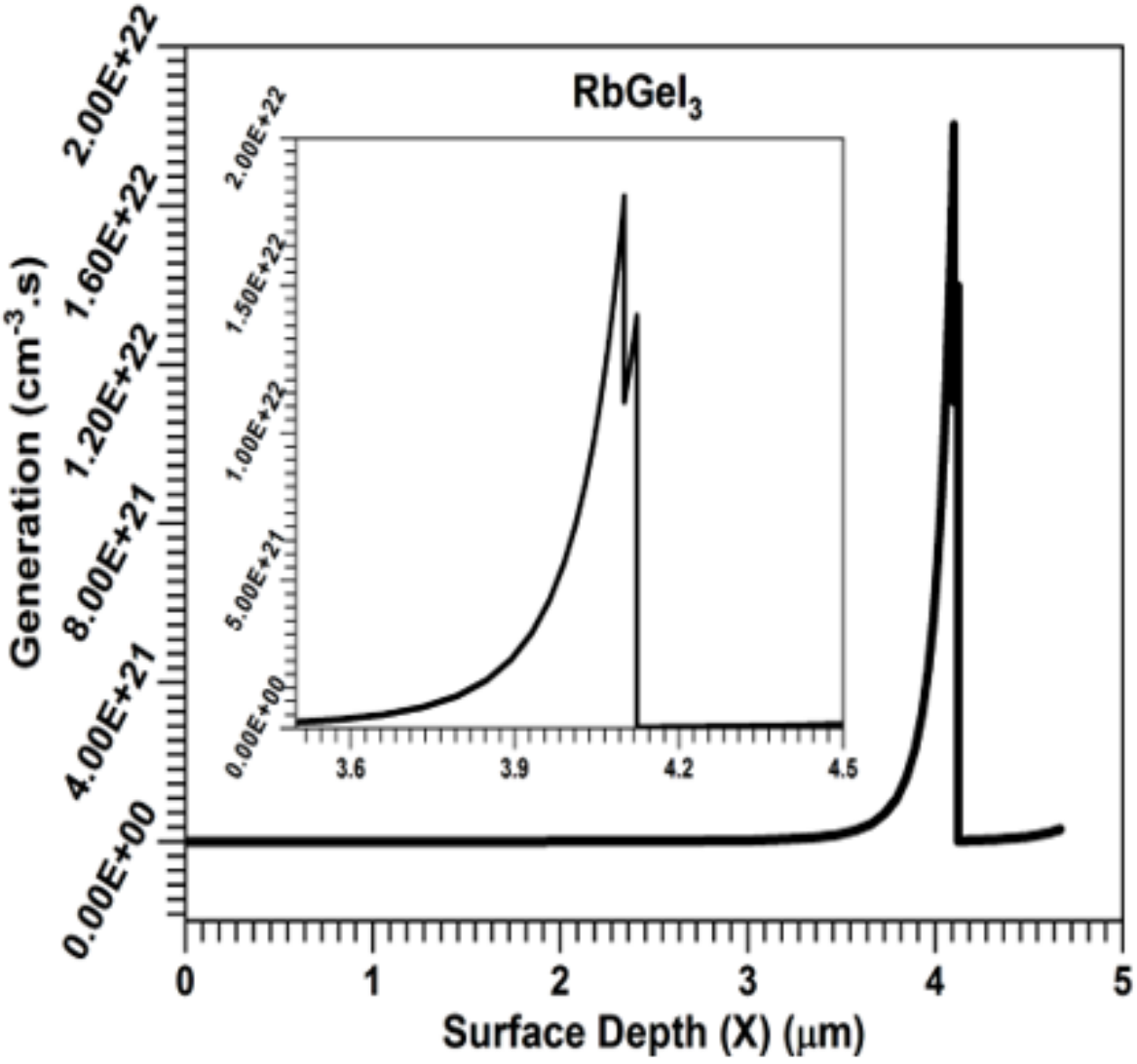

Figure 7. Generation rate

 doi:10.20944/preprints202404.0138.v1

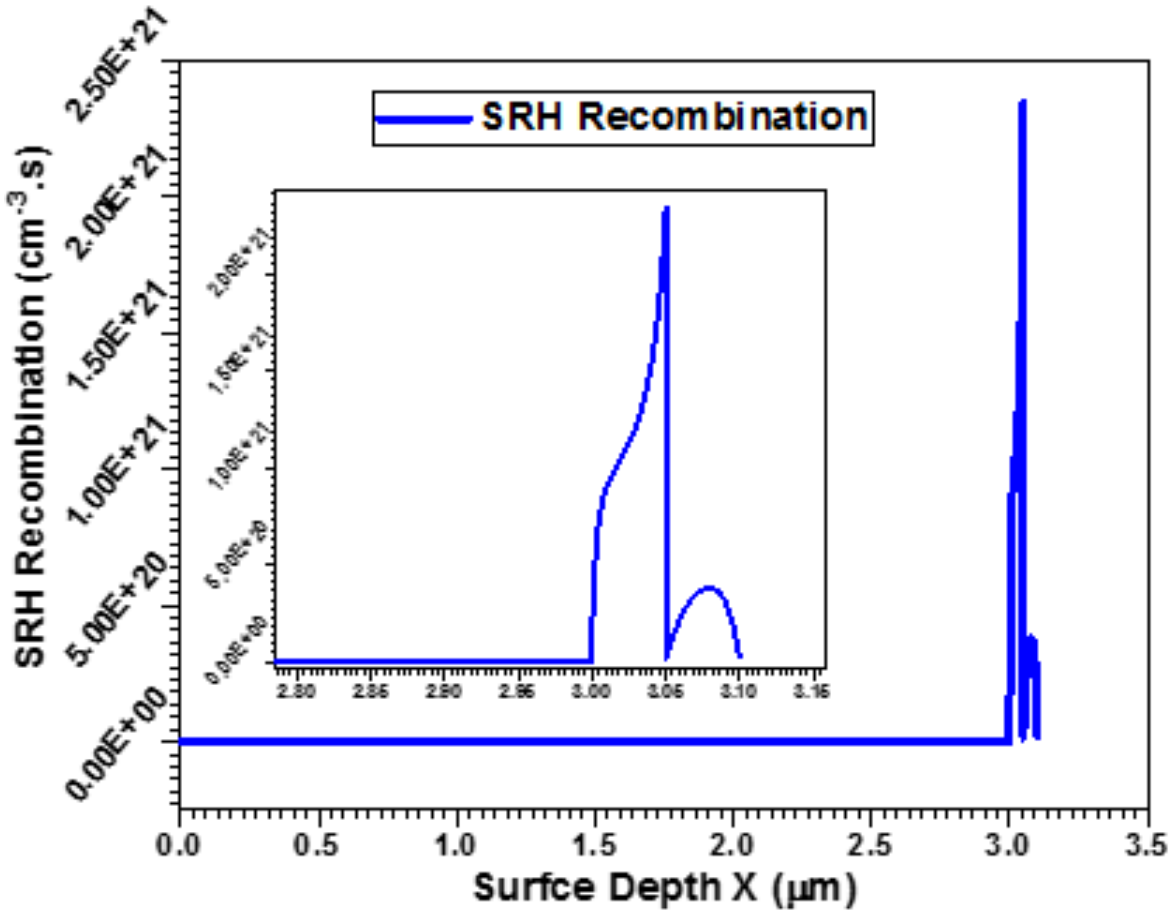

Figure 8. S_{RH} recombination of $RbGeI_3$-based solar cell

The recombination process in the suggested design is modest and lies in a lower range when compared to the carrier production rate. Moreover, all re-combinations from carrier generation can be compared with the maxima value of given $2.35 \times 10^{21} cm^{-3}s$ at a depth of $3.05m$ as shown in Figure 8.

3.7. Effect of $RbGeI_3$ Absorber Layer Thickness

The absorber layer and its thickness fluctuation are critical to the performance of PV devices. The thickness of the $RbGeI_3$ absorber layer was changed from $1.5\mu m$ to $4.5\mu m$. The effect of each different thickness on the PV cell $J-V$ characteristics curve was significant. The enhancement in the thickness of the PV absorbing layer can give more space for photons captured from solar irradiance. As a result, its similar impact can be shown in Figure 9, 10, and Table 3.

V_{oc} was measured at $0.945958V$ at a thickness of $1.5\mu m$; however, by increasing thickness to $2.0\mu m$, the V_{oc} decreased to $0.9457V$ as shown in Figure 10. After gradually increasing the thickness up to $4.5\mu m$, the V_{oc} also increases from $0.94583V$, to $0.94595V$. The overall conclusion from the scenario is that increased thickness causes improvement in current density, however, at $1.5\mu m$ the current density of $34.525mA/cm^2$ is measured, and after that, an increase in thickness affects the current density very slowly; initially, it goes down and then increases and reaches $34.525mA/cm^2$ at $4.5\mu m$ of thickness. The optimized thickness of the cell is proposed at $1.5\mu m$, at which PCE also increased, and its difference is minor with a thickness of $3\mu m$. For the (FF) of the solar cell, it's also observed that there is an enhancement, as originally at $1.5\mu m$ it was 77.7773%, later on, on other thicknesses such as $2\mu m$, $2.5\mu m$, $3\mu m$, and $3.5\mu m$, $4\mu m$, $4.5\mu m$ it was computed as 77.7812%, 77.7797%, 77.7787%, and 77.7781%, 77.7778%, 77.7773%. Furthermore, it has been shown that raising an absorber layer's thickness enhances both V_{oc} and J_{sc} since doing so expands the absorber layer's surface area, which boosts the generation of current in PV cells. However, the increasing thickness also raises the cell's

 doi:10.20944/preprints202404.0138.v1

resistance, which can cause a rise in the V_{oc} of the PV cell. Finally, the efficiency ranges from 25.29% to 25.40%, indicating a significant increase in the $RbGeI_3$-based PSC PCE. Moreover, the PCE was 25.40% at the given thickness of 1.5μm, where at 2μm it was 25.29%, at 2.5μm it was 25.34%, at 3μm it was 25.36%, at 3.5μm it got up to 25.38%, at 4μm it reached up to 25.39%, and at 4.5μm it reached up to 25.40%.

Table 3. Effect of absorber layer thickness upon characteristics parameters

$RbGeI_3$ Thickness (μm)	V_{oc} (V)	J_{sc} (mA/cm^2)	FF (%)	η (%)
1.5	0.945958	34.52525	77.7773	25.4016
2	0.945743	34.39043	77.7812	25.298
2.5	0.945834	34.44852	77.7797	25.3427
3.0	0.945881	34.47795	77.7787	25.3652
3.5	0.945913	34.49748	77.7781	25.3802
4.0	0.945937	34.51259	77.7778	25.3919
4.5	0.945958	34.52525	77.7773	25.4016

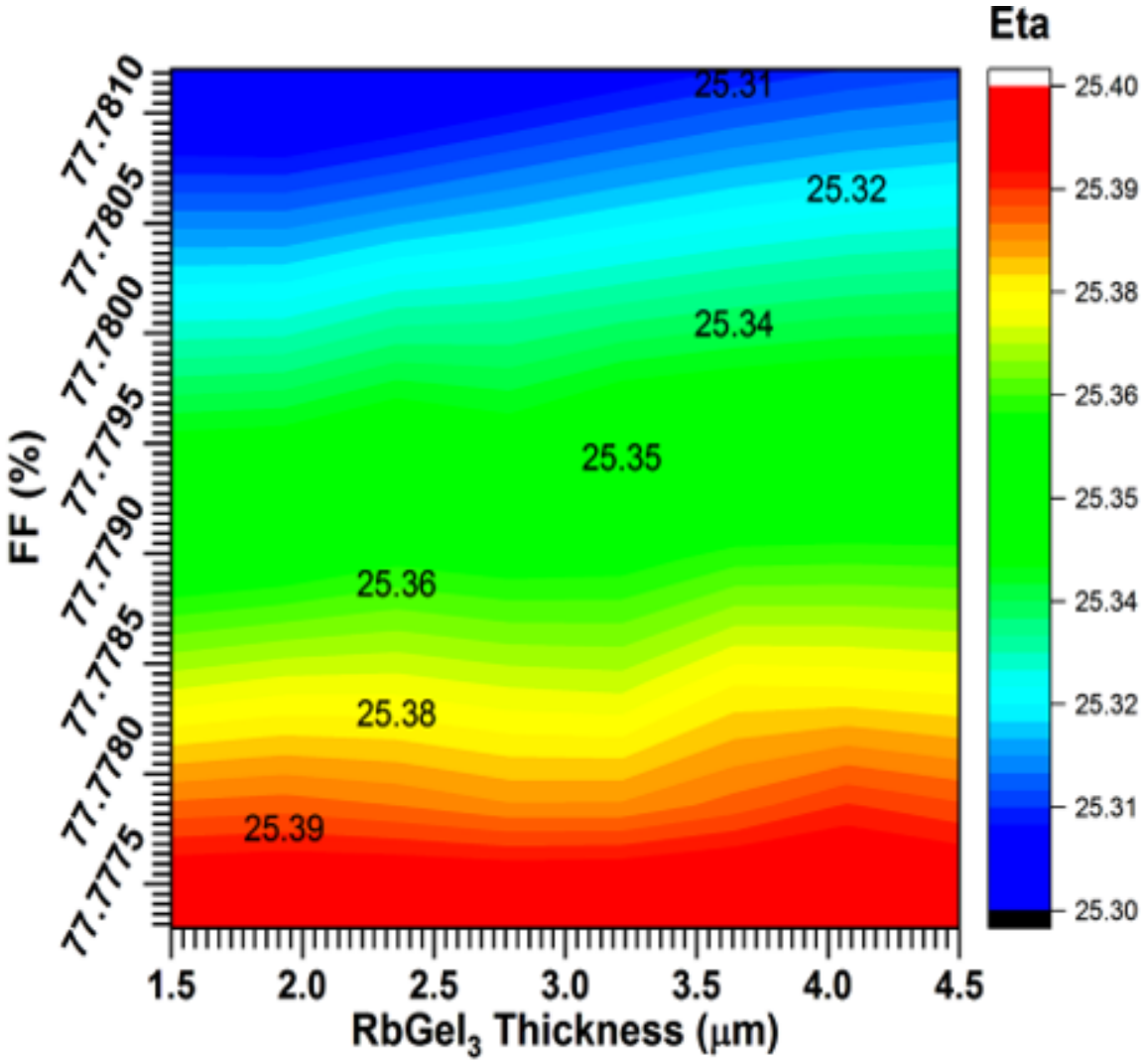

Figure 9. Effect of absorber layer thickness on the characteristics parameters of solar cell

Preprints.org (www.preprints.org) | NOT PEER-REVIEWED | Posted: 2 April 2024 doi:10.20944/preprints202404.0138.v1

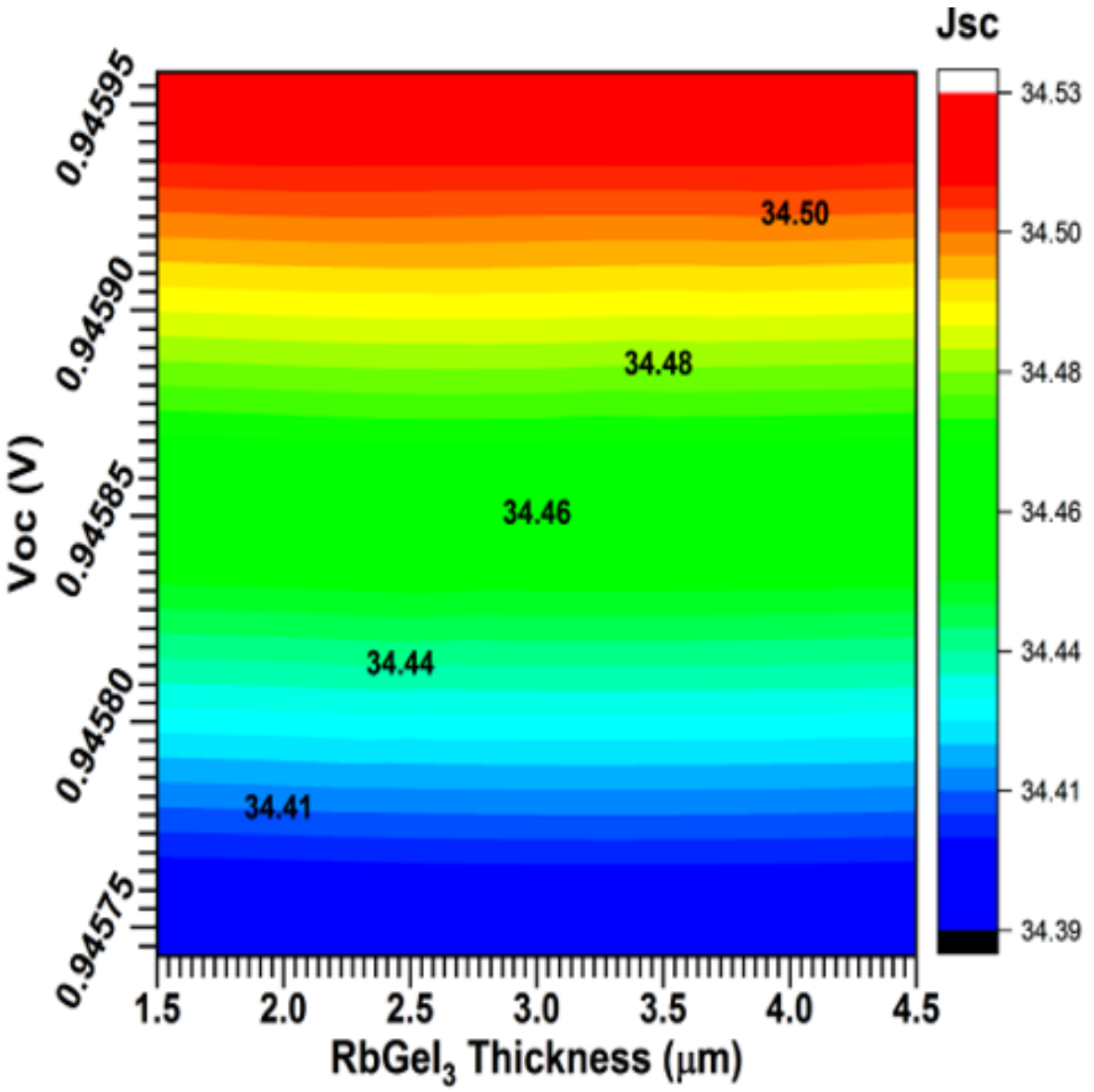

Figure 10. Effect of absorber layer thickness on the characteristics parameters of solar cell

3.8. Effect of N_d Level of Layer

The CdS layer's N_d level is seen in the simulation, where its values range from $1.00 \times 10^{20} cm$ to $1.00 \times 10^{22} cm$. The features of the proposed solar cell, like V_{oc}, J_{sc}, FF, and η, were also affected by changing the value of N_d, i.e., from $1.00 \times 10^{20} cm$ to $1.00 \times 10^{22} cm$ as shown in Table 4.

Table 4. Effect of N_d level of ZnO upon characteristic parameters of solar cell

N_d **Level of** ZnO $(1/cm^3)$	V_{oc} (V)	J_{sc} (mA/cm^2)	FF (%)	η (%)
1.00x10^{20}	1.478813	34.53617	49.7653	25.4164
1.67x10^{21}	1.486009	34.5243	49.5107	25.4007
3.33 x10^{21}	1.486043	34.52426	49.5095	25.4006
5.00 x10^{21}	1.486059	34.52425	49.5089	25.4006
6.67 x10^{21}	1.486068	34.52424	49.5086	25.4006
8.33 x10^{21}	1.486075	34.52423	49.5084	25.4006
1.00 x10^{22}	1.486079	34.52423	49.5082	25.4006

 doi:10.20944/preprints202404.0138.v1

3.9. Effect of Interface Defect Level

Different interface defect layer data are acquired from the simulation tool for the verification of research work. The performance of a PSC interface defect level is used to explore the most crucial characteristic parameter, $J-V$. Changes in interface defect levels, such as increasing the defect level further to combine already created electrons and holes with more holes, can also alter the performance of PSC, as shown in Figure 11.

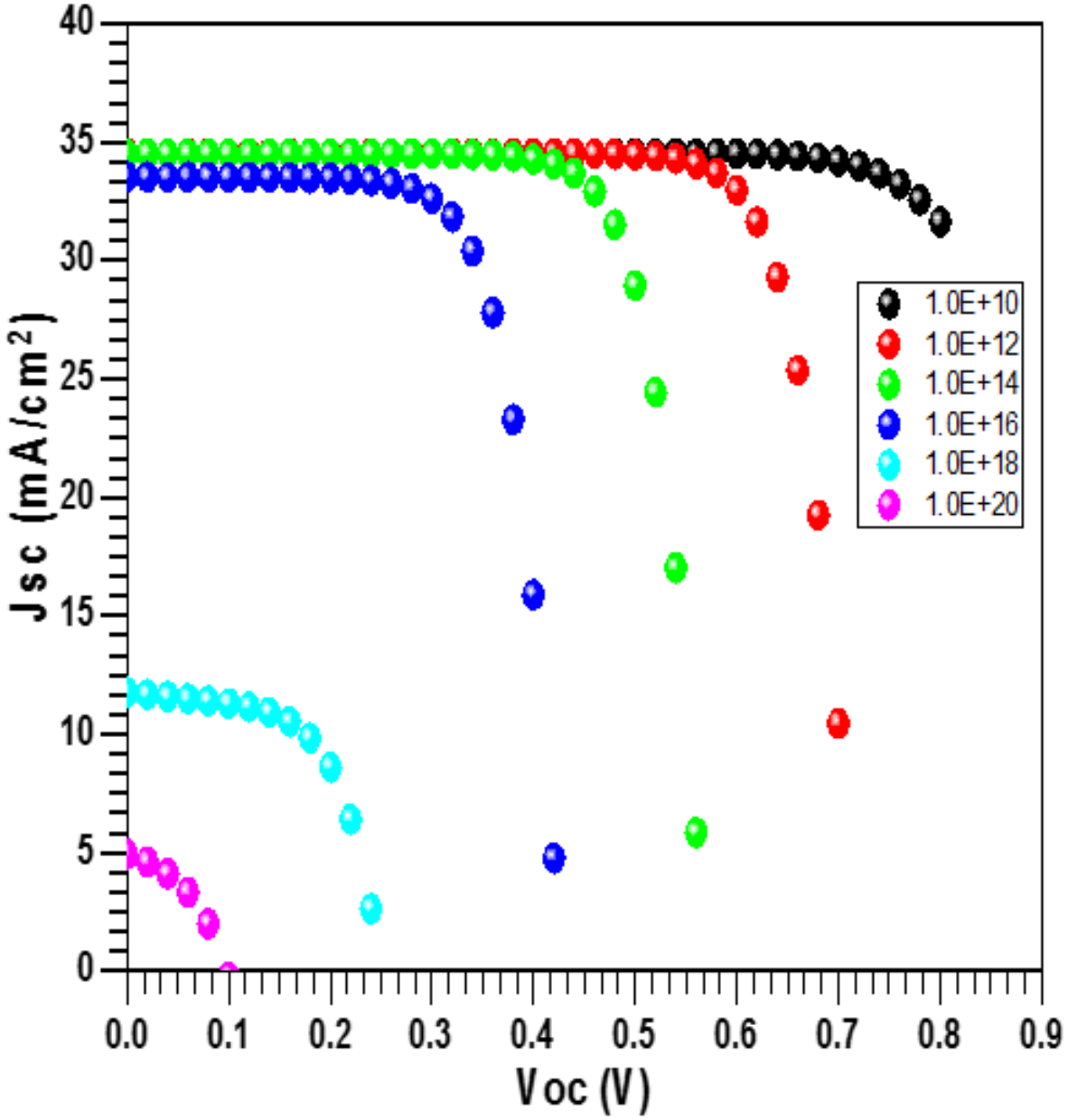

Figure 11. Effect of Interface defect level upon $J-V$ characteristic curve

3.10. Performance of Solar PV Plant using Proposed PSC

The V_{oc}, J_{sc}, FF and PCE values obtained through the optimization process of a unit area of the proposed PSC are $0.94V$, $34.52mA/cm^2$, 77.77%, and 25.40%, respectively. All of the aforementioned characteristics were entered into the PVSyst software package for at least 60 cells in a row of solar cells with a thickness of $38mm$, a weight of $27.5kg$, and a dimension of $2250mm \times 1150mm$. Different solar modules that are sold commercially come in a variety of configurations, such as 72 or more cells in

 doi:10.20944/preprints202404.0138.v1

series, but trends are moving in the direction of optimization and size reduction for ease of installation anywhere and lower transportation costs as well.

In response to incident radiation, the "$Au/CuSCN/RbGeI_3/CdTe/ZnO/TiO_2/FTO$" cell-based panel's performance is shown in Figures 12 and Figure 13. The characteristic curves clearly show that the output power increased from 92.9W to 494.2W while incident sunlight radiation varied from 200W/m^2 to 1000W/m^2. This increase in current value is due to more carriers being created with more intense lighting, which eventually increases device output. Figure 13 depicts the performance analysis of the solar module in response to temperature variation. The data clearly show that the performance of the panel degrades as the temperature increases from 10°C to 70°C degrees Celsius. The device's temperature response has been computed using incident light that is 1000W/m^2 as standard. The module's results show a similar pattern to those of a single $ITO/ZnO/CdTe/CH_3NH_3SnI_3/CuSCN/Au$ cell. Temperature increases are accompanied by a decrease in voltage and current as well as a minor increase in the value of the FF.

The device is seen to operate most effectively under typical temperature and light-source circumstances. The device's performance may suffer as the temperature continues to rise. Using the PVSyst software, we conducted theoretical analyses before simulating the solar cell device model for location computations in real-time. Being in Pakistan, we decided to place the output of the device in Islamabad and compute the profile of power of the cell over time. Our proposed solar module has been used to simulate a solar cell system with a 1$MWAC$/1.2$MWDC$ capacity. The proposed system for Islamabad is a single-axis tracker with a nine-meter pitch. The results of simulations are examined for a variety of criteria, including performance ratio, specific production, and total energy generated annually. Ω losses, light-induced degradation (LID) losses, soiling losses, auxiliaries, and shading losses are also assumed for the system to make the simulation more realistic.

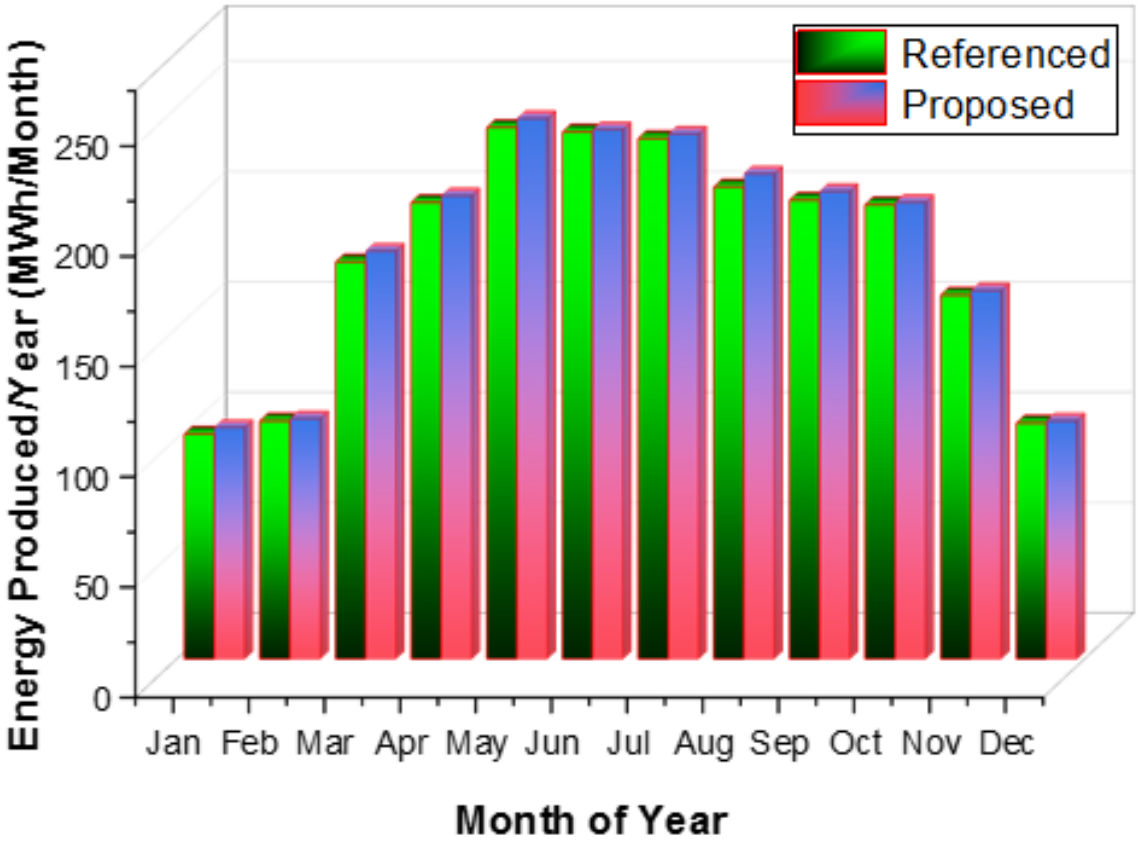

Figure 12. Energy Produced in a year by a solar module for 1 MW AC/1.2 MW DC solar PV plant

 doi:10.20944/preprints202404.0138.v1

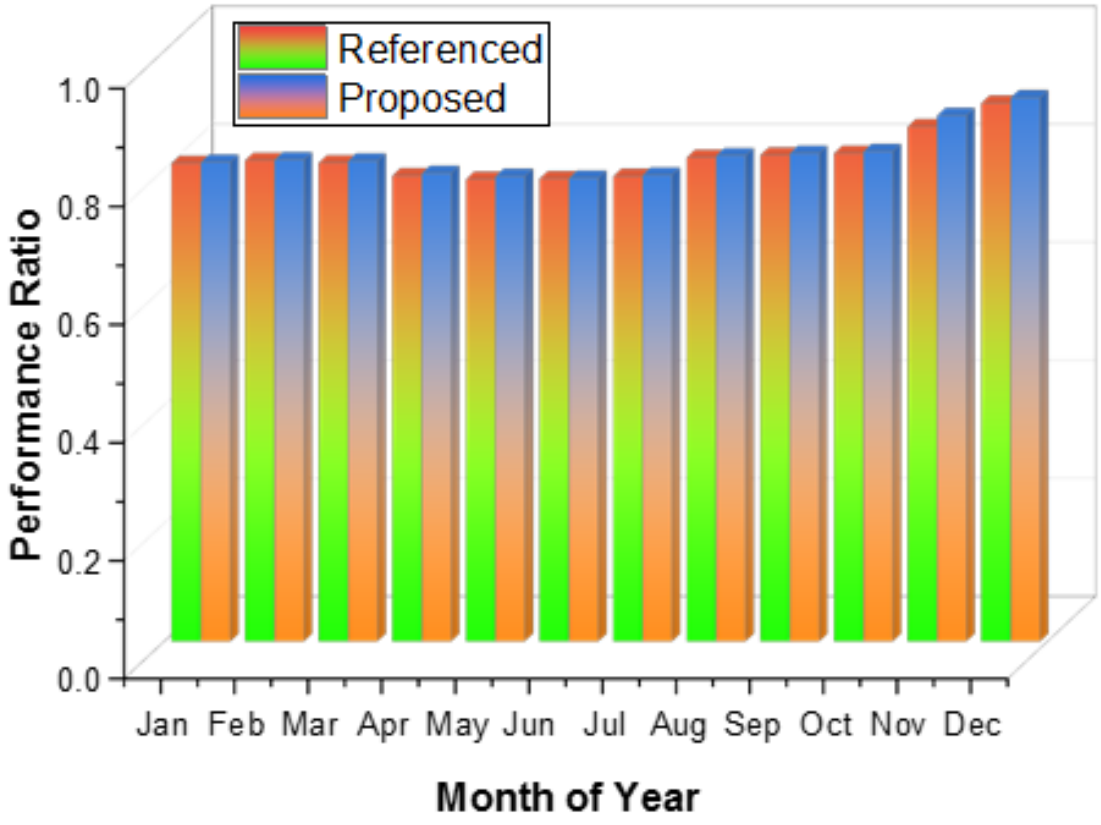

Figure 13. Monthly performance ratio of proposed solar panel in a year

4. Conclusion

The research has unveiled an innovative and lead-free solar cell model, utilizing perovskite-based technology with $RbGeI_3$ in an n-i-p planar configuration. Extensive simulations conducted with SCAPS-1D software provided valuable insights into the performance of different HTL and ETL materials, as well as their thicknesses, perovskite layer thicknesses, and doping concentrations in the layers. The optimization efforts yielded remarkable results, showcasing characteristic parameters of V_{oc} at $0.94V$, a current density of $34.52mA/cm^2$, an impressive power conversion efficiency of 25.40%, and a noteworthy (FF) of 77.77% for the proposed PSC design "$Au/CuSCN/RbGeI_3/CdTe/ZnO/TiO_2/FTO$". To assess its real-world feasibility, the calculated outcomes were integrated into the PVSyst software, resulting in a module comprising 60 solar cells arranged in series. The module generated a remarkable $512W$ of useful output power under direct and indirect irradiance of $1000W/m^2$ at ambient temperature. Notably, the solar cell exhibited sensitivity to shadows or reduced incident sunlight, indicating its responsiveness to environmental factors. The standalone PV system incorporating this optimized module achieved an annual energy generation of $2200MWh$, with an accurate output of $1829kWh/kWp$, and an exceptional performance ratio (PR) of 85.6%. This PR outperformed the reference model "$CuSCN/CH_3NH_3SnI_3/CdTe/ZnO/TiO_2/FTO$", which had a PR of 83%. This research represents a significant advancement in the field of PV, offering an eco-friendly and high-efficiency solar cell solution for modern applications. The practicality of the optimized cell design tailored to specific geographic locations further underscores its significance and real-world applicability. With its outstanding power conversion efficiency and environmental benefits, the proposed " $Au/CuSCN/RbGeI_3/CdTe/ZnO/TiO_2/FTO$" configuration signifies a promising step towards a cleaner and more sustainable future in PV technology. The research's contribution paves the way for cleaner energy solutions, making a lasting impact on the forefront of PV innovation.

 doi:10.20944/preprints202404.0138.v1

Author Contributions: Conceptualization, M.M. K and S.A.; methodology, M.M. K, A. H and S.A.; software, M.M. K; validation, M.M. K, A. H and S.A.; formal analysis, M.M. K and S.A.; investigation, M.M. K; resources, F. S.; data curation, A.H.; writing—original draft preparation, M.M. K and S.A.; writing—review and editing, A.H and F.S.; visualization, M.M. K and S.A; supervision, S.A.; project administration, F.S and S.A.; funding acquisition, A. H. All authors have read and agreed to the published version of the manuscript.

Conflicts of Interest: The authors declare no conflicts of interest.

References

1. Ang, T.Z.; Salem, M.; Kamarol, M.; Das, H.S.; Nazari, M.A.; Prabaharan, N. A comprehensive study of renewable energy sources: classifications, challenges and suggestions. *Energy Strategy Reviews* **2022**, *43*, 100939.
2. Nieto-Diaz, B.A.; Pearson, C.; Al-Busaidi, Z.; Bowen, L.; Petty, M.C.; Groves, C. Enhanced lifetime of organic photovoltaic diodes achieved by blending with PMMA: Impact of morphology and Donor: Acceptor combination. *Solar Energy Materials and Solar Cells* **2021**, *219*, 110765.
3. Ghosh, S.; Singh, T. Role of ionic liquids in organic-inorganic metal halide perovskite solar cells efficiency and stability. *Nano Energy* **2019**, *63*, 103828.
4. Wu, T.; Qin, Z.; Wang, Y.; Wu, Y.; Chen, W.; Zhang, S.; Cai, M.; Dai, S.; Zhang, J.; Liu, J.; others. The main progress of perovskite solar cells in 2020–2021. *Nano-Micro Letters* **2021**, *13*, 1–18.
5. Ke, W.; Kanatzidis, M.G. Prospects for low-toxicity lead-free perovskite solar cells. *Nature communications* **2019**, *10*, 965.
6. Noel, N.K.; Stranks, S.D.; Abate, A.; Wehrenfennig, C.; Guarnera, S.; Haghighirad, A.A.; Sadhanala, A.; Eperon, G.E.; Pathak, S.K.; Johnston, M.B.; others. Lead-free organic–inorganic tin halide perovskites for photovoltaic applications. *Energy & Environmental Science* **2014**, *7*, 3061–3068.
7. Wang, D.; Wright, M.; Elumalai, N.K.; Uddin, A. Stability of perovskite solar cells. *Solar Energy Materials and Solar Cells* **2016**, *147*, 255–275.
8. Roknuzzaman, M.; Ostrikov, K.; Wang, H.; Du, A.; Tesfamichael, T. Towards lead-free perovskite photovoltaics and optoelectronics by ab-initio simulations. *Scientific reports* **2017**, *7*, 14025.
9. Sabba, D.; Mulmudi, H.K.; Prabhakar, R.R.; Krishnamoorthy, T.; Baikie, T.; Boix, P.P.; Mhaisalkar, S.; Mathews, N. Impact of anionic Br–substitution on open circuit voltage in lead free perovskite (CsSnI3-xBr x) solar cells. *The journal of physical chemistry C* **2015**, *119*, 1763–1767.
10. Kumar, A.; Kumar, V.; Prajapati, R.; Asthana, S.K.; Upadhyay, K.; Zhao, J.; others. A remarkable effect of N, N-diethylamino functionality on the optoelectronic properties of a salicyl imine-based probe for Al 3+. *Dalton Transactions* **2014**, *43*, 5831–5839.
11. Bu, T.; Wu, L.; Liu, X.; Yang, X.; Zhou, P.; Yu, X.; Qin, T.; Shi, J.; Wang, S.; Li, S.; others. Synergic interface optimization with green solvent engineering in mixed perovskite solar cells. *Advanced Energy Materials* **2017**, *7*, 1700576.
12. Kwak, J.I.; Lee, T.Y.; An, Y.J. Assessing the potential toxicity of hazardous material released from Pb-based perovskite solar cells to crop plants. *Journal of Cleaner Production* **2023**, *423*, 138856.
13. Gao, Z.; Chen, S.; Bai, Y.; Wang, M.; Liu, X.; Yang, W.; Li, W.; Ding, X.; Yao, J. A new perspective for evaluating the photoelectric performance of organic–inorganic hybrid perovskites based on the DFT calculations of excited states. *Physical Chemistry Chemical Physics* **2021**, *23*, 11548–11556.
14. Pindolia, G.; Shinde, S.M.; Jha, P.K. Optimization of an inorganic lead free RbGeI3 based perovskite solar cell by SCAPS-1D simulation. *Solar Energy* **2022**, *236*, 802–821.
15. Shafi, M.A.; Khan, M.; Bibi, S.; Shafi, M.Y.; Rabbani, N.; Ullah, H.; Khan, L.; Mari, B. Effect of parasitic parameters and environmental conditions on IV and PV characteristics of 1D5P model solar PV cell using LTSPICE-IV. *East European Journal of Physics* **2022**, pp. 64–74.
16. Deepthi Jayan, K. Design and Comparative Performance Analysis of High-Efficiency Lead-Based and Lead-Free Perovskite Solar Cells. *physica status solidi (a)* **2022**, *219*, 2100606.
17. Jayan K, D.; Sebastian, V. Comparative study on the performance of different Lead-based and Lead-free perovskite solar cells. *Advanced Theory and Simulations* **2021**, *4*, 2100027.
18. Parrey, K.A.; Farooq, T.; Khandy, S.A.; Farooq, U.; Gupta, A. First principle studies on structure, magneto-electronic and elastic properties of photovoltaic semiconductor halide (RbGeI3) and ferromagnetic half metal oxide (RbDyO3). *Computational Condensed Matter* **2019**, *19*, e00381.

 doi:10.20944/preprints202404.0138.v1

19. Khurshid, S.; Latif, H.; Rasheed, S.; Sharif, R.; Sattar, A.; Amjad, R. Enhancement in absorption spectrum by ITO coated, down converting glass as a photoanode substrate for efficient PbS/CdS quantum dots sensitized ZnO nano-rods array solar cell. *Optical Materials* **2022**, *124*, 111991.
20. Shafi, M.A.; Bibi, S.; Khan, M.M.; Sikandar, H.; Javed, F.; Ullah, H.; Khan, L.; Mari, B. A numerical simulation for efficiency enhancement of CZTS-based thin film solar cell using SCAPS-1D. *East European Journal of Physics* **2022**, pp. 52–63.
21. Jong, U.G.; Yu, C.J.; Kye, Y.H.; Choe, Y.G.; Hao, W.; Li, S. First-principles study on structural, electronic, and optical properties of inorganic Ge-based halide perovskites. *Inorganic chemistry* **2019**, *58*, 4134–4140.
22. Wang, Z.; Jiang, Y. Advances in perovskite solar cells: film morphology control and interface engineering. *Journal of Cleaner Production* **2021**, *317*, 128368.
23. Ju, M.G.; Chen, M.; Zhou, Y.; Dai, J.; Ma, L.; Padture, N.P.; Zeng, X.C. Toward eco-friendly and stable perovskite materials for photovoltaics. *Joule* **2018**, *2*, 1231–1241.
24. Leijtens, T.; Eperon, G.E.; Noel, N.K.; Habisreutinger, S.N.; Petrozza, A.; Snaith, H.J. Stability of metal halide perovskite solar cells. *Advanced Energy Materials* **2015**, *5*, 1500963.
25. Allouhi, A.; Rehman, S.; Buker, M.S.; Said, Z. Up-to-date literature review on Solar PV systems: Technology progress, market status and R&D. *Journal of Cleaner Production* **2022**, *362*, 132339.
26. Saragi, T.P.; Spehr, T.; Siebert, A.; Fuhrmann-Lieker, T.; Salbeck, J. Spiro compounds for organic optoelectronics. *Chemical reviews* **2007**, *107*, 1011–1065.
27. Tour, J.M.; Wu, R.; Schumm, J.S. Approaches to orthogonally fused conducting polymers for molecular electronics. *Journal of the American Chemical Society* **1990**, *112*, 5662–5663.
28. Abdellah, I.M.; Chowdhury, T.H.; Lee, J.J.; Islam, A.; Nazeeruddin, M.K.; Gräetzel, M.; El-Shafei, A. Facile and low-cost synthesis of a novel dopant-free hole transporting material that rivals Spiro-OMeTAD for high efficiency perovskite solar cells. *Sustainable Energy & Fuels* **2021**, *5*, 199–211.
29. Wang, J.; Zhao, P.; Hu, Y.; Lin, Z.; Su, J.; Zhang, J.; Chang, J.; Hao, Y. An Exploration of All-Inorganic Perovskite/Gallium Arsenide Tandem Solar Cells. *Solar RRL* **2021**, *5*, 2100121.
30. Zhao, P.; Liu, Z.; Lin, Z.; Chen, D.; Su, J.; Zhang, C.; Zhang, J.; Chang, J.; Hao, Y. Device simulation of inverted CH3NH3PbI3- xClx perovskite solar cells based on PCBM electron transport layer and NiO hole transport layer. *Solar Energy* **2018**, *169*, 11–18.
31. Zhao, P.; Su, J.; Lin, Z.; Wang, J.; Zhang, J.; Hao, Y.; Ouyang, X.; Chang, J. All-Inorganic CsPbIxBr3- x perovskite solar cells: crystal anisotropy effect. *Advanced Theory and Simulations* **2020**, *3*, 2000055.
32. Zhao, P.; Lin, Z.; Wang, J.; Yue, M.; Su, J.; Zhang, J.; Chang, J.; Hao, Y. Numerical simulation of planar heterojunction perovskite solar cells based on SnO2 electron transport layer. *ACS Applied Energy Materials* **2019**, *2*, 4504–4512.
33. Ru, X.; Qu, M.; Wang, J.; Ruan, T.; Yang, M.; Peng, F.; Long, W.; Zheng, K.; Yan, H.; Xu, X. 25.11% efficiency silicon heterojunction solar cell with low deposition rate intrinsic amorphous silicon buffer layers. *Solar energy materials and solar cells* **2020**, *215*, 110643.
34. Liang, J.; Wang, C.; Wang, Y.; Xu, Z.; Lu, Z.; Ma, Y.; Zhu, H.; Hu, Y.; Xiao, C.; Yi, X.; others. All-inorganic perovskite solar cells. *Journal of the American Chemical Society* **2016**, *138*, 15829–15832.
35. Ouedraogo, N.A.N.; Chen, Y.; Xiao, Y.Y.; Meng, Q.; Han, C.B.; Yan, H.; Zhang, Y. Stability of all-inorganic perovskite solar cells. *Nano Energy* **2020**, *67*, 104249.
36. Singh, R.; Singh, P.K.; Bhattacharya, B.; Rhee, H.W. Review of current progress in inorganic hole-transport materials for perovskite solar cells. *Applied Materials Today* **2019**, *14*, 175–200.
37. Wei, H.; Qiu, P.; Li, Y.; He, Y.; Peng, M.; Zheng, X.; Liu, X. Challenges and strategies of all-inorganic lead-free halide perovskite solar cells. *Ceramics International* **2022**, *48*, 5876–5891.
38. Li, R.; Hassan, A.; Gupte, N.; Su, W.; Zhou, X. Degradation Prediction and Cost Optimization of Second-Life Battery Used for Energy Arbitrage and Peak-Shaving in an Electric Grid. *Energies* **2023**, *16*, 6200.
39. Hassan, A.; Khan, S.A.; Li, R.; Su, W.; Zhou, X.; Wang, M.; Wang, B. Second-Life Batteries: A Review on Power Grid Applications, Degradation Mechanisms, and Power Electronics Interface Architectures. *Batteries* **2023**, *9*, 571.
40. Beg, O.A.; Khan, A.A.; Rehman, W.U.; Hassan, A. A Review of AI-Based Cyber-Attack Detection and Mitigation in Microgrids. *Energies* **2023**, *16*, 7644.

 doi:10.20944/preprints202404.0138.v1

41. Qasim, I.; Ahmad, O.; ul Abdin, Z.; Rashid, A.; Nasir, M.F.; Malik, M.I.; Rashid, M.; Hasnain, S.M. Design and numerical investigations of eco-friendly, non-toxic (Au/CuSCN/CH3NH3SnI3/CdTe/ZnO/ITO) perovskite solar cell and module. *Solar Energy* **2022**, *237*, 52–61.